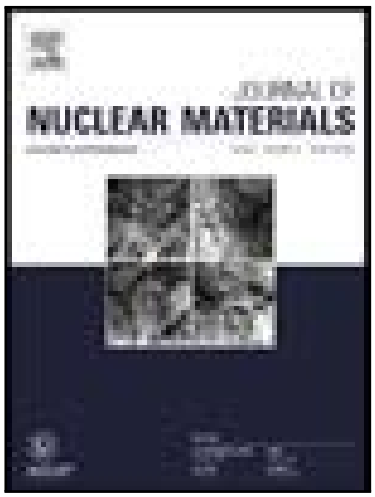

Application of the Immobilized Low-Activity Waste Glass Corrosion Model to the Static Dissolution of 24 Statistically-Designed Alkali-Borosilicate Waste Glasses

Sebastien N. Kerisit , James J. Neeway , Charmayne E. Lonergan , Benjamin Parruzot , Jarrod V. Crum , Richard C. Daniel , Gary L. Smith , R. Matthew Asmussen

PII: S0022-3115(24)00071-0
DOI: https://doi.org/10.1016/j.jnucmat.2024.154968
Reference: NUMA 154968

To appear in: *Journal of Nuclear Materials*

Received date: 5 November 2023
Revised date: 22 January 2024
Accepted date: 10 February 2024

Please cite this article as: Sebastien N. Kerisit , James J. Neeway , Charmayne E. Lonergan , Benjamin Parruzot , Jarrod V. Crum , Richard C. Daniel , Gary L. Smith , R. Matthew Asmussen , Application of the Immobilized Low-Activity Waste Glass Corrosion Model to the Static Dissolution of 24 Statistically-Designed Alkali-Borosilicate Waste Glasses, *Journal of Nuclear Materials* (2024), doi: https://doi.org/10.1016/j.jnucmat.2024.154968

Application of the Immobilized Low-Activity Waste Glass Corrosion Model to the Static Dissolution of 24 Statistically-Designed Alkali-Borosilicate Waste Glasses

Sebastien N. Kerisit[1,*], *James J. Neeway*[2], *Charmayne E. Lonergan*[3], *Benjamin Parruzot*[2], *Jarrod V. Crum*[2], *Richard C. Daniel*[2], *Gary L. Smith*[2], *and R. Matthew Asmussen*[2]

[1]Physical and Computational Sciences Directorate, Pacific Northwest National Laboratory, Richland, Washington 99352, United States

[2]Energy and Environment Directorate, Pacific Northwest National Laboratory, Richland, Washington 99352, United States

[3]Materials Science and Engineering Department, Missouri University of Science and Technology, Rolla, Missouri 65409, United States

February 11, 2024

ABSTRACT

Glass corrosion models that capture the complex mechanisms of the glass-water reaction enable the prediction of nuclear waste glass durability in disposal scenarios. Parameterization of such models is challenging because of the need to capture changes in corrosion behavior with time, reaction conditions, and glass composition. Here, we describe and employ the ILAW (immobilized low-activity waste) glass corrosion model (IGCM) in geochemical simulations of static dissolution tests, at two temperatures (40 °C and 90 °C), for a matrix of 24 enhanced low-activity waste (eLAW) glasses statistically designed to cover a processable composition space defined by 8 major glass components (Al_2O_3, B_2O_3, CaO, Na_2O, SiO_2, SnO_2, ZrO_2, and Others as defined in the text). The IGCM includes a first-order chemical affinity term and an ion-exchange term that represents the net exchange of Na^+ ions in the pristine glass with protons in aqueous solution. Constant, time-dependent, and time- and pH-dependent functional forms of the ion-exchange term are evaluated to reproduce the change in corrosion behavior with time in saturated, static dissolution tests. The agreement with measured aqueous concentrations of the main glass components (B, Na, and Si) improved significantly upon addition of a time-dependent term, which therefore constitutes a simple representation of the glass-water reaction progress. Due to the limited changes in pH in the static dissolution tests, past a short initial period of rapid increase, addition of a pH-dependent term did not appreciably improve the fits, indicating that comprehensive model parameterization requires more than one type of glass corrosion test to capture a wide range of solution chemistries. IGCM parameters were found to be dependent on glass composition, and the parameter sets generated in this work will enable the development of composition–parameter correlation models that offer the promise of predicting IGCM parameters, and thus glass corrosion behavior, solely based on glass composition.

INTRODUCTION

Immobilization of radionuclides through vitrification in borosilicate glass is a strategy pursued internationally for safe and long-term disposal of nuclear waste (Gin et al. 2013). Assessments of the potential long-term impacts on human health and the environment of disposal facilities rely in large part on the accuracy of nuclear waste glass corrosion models (Vienna et al. 2013; Frankel et al. 2021). The corrosion of borosilicate glass in aqueous solution is often described as consisting of three stages (Gin et al. 2013; Vienna et al. 2013; Frankel et al. 2021). In Stage I, glass initially dissolves rapidly in dilute conditions and, as the concentration of dissolved glass components builds up in solution, the glass dissolution rate progressively slows down. The glass dissolution rate reaches a lower and approximately constant residual rate, which is defined as Stage II. The precipitation of secondary phases, in particular aluminosilicate phases such as zeolites, can trigger an acceleration of the glass dissolution rate (Van Iseghem and Grambow 1987; Patyn et al. 1990; Ebert et al. 1992; Ribet and Gin 2004; Neeway et al. 2020; Crum et al. 2021; Parruzot et al. 2022), which is referred to as Stage III. In a typical disposal scenario, glass is expected to spend most, if not almost all, of its lifetime in Stage II.

Models of glass corrosion generally treat the slowing down of the glass dissolution rate between Stage I and Stage II as an approach to pseudo-equilibrium via a chemical affinity term with the functional form derived by Åagaard and Helgeson (1982) for silicate minerals. However, because glass is metastable in aqueous conditions, thermodynamic equilibrium between the glass and solution is not possible, and an additional process is needed to model the residual corrosion rate (or Stage II rate). Because the mechanisms of glass corrosion are extremely complex and have yet to be fully resolved, glass corrosion models have used an empirical term to model the residual corrosion rate. For example, shortly after developing his

first-order rate equation in 1985 (Grambow 1985) based on the work of Åagaard and Helgeson (1982), Grambow added a constant "final rate of reaction" to prevent the glass dissolution reaction from stopping once the equilibrium silicic acid concentration was reached (Grambow 1987). In another example, the GRAAL (glass reactivity in allowance for the alteration layer) model developed by Frugier and co-workers (Frugier et al. 2008; Frugier et al. 2009; Frugier et al. 2018) at the French Alternative and Atomic Energy Commission (CEA), and also employed by other research groups (Rieke et al. 2018), accounts for the decrease of the glass dissolution rate via a thickness-dependent rate of formation of a passivating reactive interphase (PRI) atop the pristine glass. In the ILAW (immobilized low-activity waste) glass corrosion model (IGCM)—developed in the late 1990s in the context of the performance assessment (PA) of the Integrated Disposal Facility (IDF), a low-activity waste repository (McGrail et al. 2001) located on the Hanford Site in Washington state, USA—the glass-water reaction is prevented from reaching pseudo-equilibrium through the addition of an ion-exchange (IEX) reaction between Na^+ ions in the pristine glass and protons in the aqueous solution. A constant IEX rate has been assumed in the IGCM previously (McGrail et al. 2001); however, a constant rate may not be the most adequate representation. The ion-exchange reaction is known to be a diffusive process (Doremus 1964; Doremus 1975; Feng et al. 1990; Ojovan et al. 2006; Neeway et al. 2014; Neeway et al. 2016), which should cause the flux of Na^+ ions out of the glass to diminish with time as the IEX front penetrates the glass and the path for Na^+ ions to diffuse out of the glass lengthens accordingly. This work therefore aims to evaluate alternative functional forms of the IEX term of the IGCM that add either time dependence to the model or both time and pH dependence.

This evaluation is achieved via geochemical calculations that apply the IGCM in fits to static dissolution test data (Crum et al. 2022; Neeway et al. 2023b), at two temperatures (40 °C and 90 °C), for 24 alkali-borosilicate glasses, referred to as the enhanced low-activity waste (eLAW) glasses. The eLAW glass matrix is a statistically designed matrix of glass compositions developed to provide uniform coverage of a the composition of glasses that could be processed in a vitrification facility for LAW defined by 8 glass components anticipated to have controlling effects over glass dissolution: Al_2O_3, B_2O_3, CaO, Na_2O, SiO_2, SnO_2, ZrO_2, and Others (Others consists of 10 glass components whose relative proportions were kept fixed in the matrix design, Table 1) (Crum et al. 2021). In addition to providing a quantitative determination of the range of IGCM parameters and glass corrosion behaviors over a wide glass composition space, the eLAW matrix enables the development of composition–parameter correlation (CPC) models that predict IGCM parameters, and consequently glass corrosion behavior, based on glass composition (Kerisit et al. 2022). This approach could quickly be applied to other glass corrosion datasets, if desired.

The best-fit parameters derived through this approach (i.e., the parameters of the IEX term as well as the glass pseudo-equilibrium constant used in the chemical affinity term) are compared to those obtained with other experimental techniques used previously to parameterize the IGCM and to equivalent parameters in other glass corrosion models such as the Grambow and Müller model (Grambow and Müller 2001), the Techer model (Techer et al. 2000), or GRAAL (Frugier et al. 2008; Frugier et al. 2009; Frugier et al. 2018). This comparison allows an evaluation of the effects of test conditions on the values of glass corrosion model parameters.

Table 1. Composition of the eLAW glasses 1 through 12 (mole fractions). The glass components comprised in 'Others' are shown with gray background.

	01	02	03	04	05	06	07	08	09	10	11	12
Al_2O_3	0.061442	0.057547	0.041074	0.059582	0.046028	0.074146	0.049077	0.041403	0.074901	0.079058	0.051040	0.057405
B_2O_3	0.064316	0.139389	0.140140	0.061434	0.164360	0.153965	0.071970	0.059010	0.095814	0.163713	0.110382	0.134899
CaO	0.015387	0.061692	0.085934	0.087320	0.002525	0.021170	0.113844	0.047731	0.079818	0.118170	0.067523	0.031252
Cl^-	0.006899	0.002799	0.002596	0.007684	0.002853	0.004426	0.005803	0.004132	0.007382	0.003402	0.004257	0.006038
Cr_2O_3	0.003442	0.001436	0.001341	0.003898	0.001464	0.002200	0.002969	0.002103	0.003665	0.001719	0.002159	0.002993
F^-	0.019313	0.008008	0.007613	0.021868	0.008163	0.012211	0.016418	0.011566	0.020841	0.009875	0.012090	0.016901
Fe_2O_3	0.004382	0.001823	0.001688	0.004905	0.001858	0.002777	0.003740	0.002669	0.004665	0.002224	0.002753	0.003812
K_2O	0.012406	0.005126	0.004816	0.013881	0.005225	0.007895	0.010567	0.007492	0.013179	0.006259	0.007802	0.010793
MgO	0.018878	0.007713	0.007339	0.021119	0.007862	0.012017	0.016134	0.011397	0.020144	0.009475	0.011884	0.016428
Na_2O	0.257626	0.260529	0.159221	0.211421	0.222157	0.201350	0.165005	0.268365	0.180821	0.169409	0.204145	0.191895
P_2O_5	0.005553	0.002284	0.002177	0.006238	0.002328	0.003557	0.004722	0.003377	0.005910	0.002785	0.003514	0.004854
SiO_2	0.449849	0.412967	0.497428	0.404434	0.481552	0.440718	0.467875	0.472421	0.424421	0.390539	0.474899	0.462131
SnO_2	0.017766	0.005092	0.002400	0.010847	0.021524	0.003577	0.009293	0.013212	0.002138	0.003113	0.001045	0.007857
SO_3	0.007299	0.001900	0.002053	0.008166	0.002695	0.004687	0.006051	0.004242	0.007795	0.002594	0.003853	0.006350
V_2O_5	0.006426	0.002655	0.002494	0.007190	0.002706	0.004089	0.005473	0.003881	0.006826	0.003242	0.004041	0.005590
ZnO	0.040249	0.016584	0.015594	0.045031	0.016905	0.025575	0.034255	0.024304	0.042804	0.020175	0.025244	0.034939
ZrO_2	0.008768	0.012455	0.026091	0.024983	0.009795	0.025638	0.016804	0.022696	0.008877	0.014247	0.013368	0.005863

Table 1 (cont.). Composition of the eLAW glasses 13 through 24 (mole fractions). The glass components comprised in 'Others' are shown with gray background.

	13	14	15	16	17	18	19	20	21	22	23	24
Al_2O_3	0.062128	0.048963	0.065725	0.039738	0.054770	0.051322	0.046444	0.047311	0.065112	0.070333	0.083044	0.040532
B_2O_3	0.117607	0.095970	0.073832	0.131137	0.060951	0.126916	0.111984	0.065652	0.093507	0.083544	0.124939	0.125168
CaO	0.100581	0.059510	0.087176	0.000356	0.100967	0.019455	0.038672	0.005465	0.042972	0.054805	0.012481	0.105585
Cl^-	0.003231	0.006366	0.003919	0.006767	0.003472	0.007219	0.007743	0.005450	0.004978	0.002424	0.005175	0.005668
Cr_2O_3	0.001641	0.003240	0.001915	0.003420	0.001748	0.003633	0.003883	0.002762	0.002501	0.001218	0.002593	0.002865
F^-	0.009222	0.017998	0.010794	0.018942	0.009889	0.020206	0.021674	0.015431	0.013935	0.006958	0.014665	0.016218
Fe_2O_3	0.002068	0.004068	0.002444	0.004298	0.002191	0.004597	0.004899	0.003463	0.003188	0.001531	0.003319	0.003649
K_2O	0.005866	0.011543	0.006952	0.012168	0.006258	0.012940	0.013842	0.009831	0.008935	0.004350	0.009378	0.010310
MgO	0.009027	0.017474	0.010503	0.018515	0.009482	0.019714	0.021111	0.014876	0.013640	0.006558	0.014160	0.015619
Na_2O	0.168422	0.238555	0.249550	0.178701	0.205081	0.243292	0.176172	0.259295	0.216860	0.241221	0.271037	0.194636
P_2O_5	0.002659	0.005203	0.003123	0.005493	0.002784	0.005836	0.006189	0.004412	0.004017	0.001956	0.004213	0.004624
SiO_2	0.459284	0.398592	0.433469	0.510192	0.504714	0.408444	0.445464	0.495128	0.459031	0.489511	0.399014	0.403104
SnO_2	0.022316	0.018607	0.000527	0.006059	0.004084	0.002458	0.014893	0.001415	0.014280	0.008904	0.007486	0.020314
SO_3	0.003114	0.006833	0.003388	0.007158	0.002994	0.007402	0.008143	0.005742	0.005257	0.002229	0.005517	0.004685
V_2O_5	0.003038	0.005978	0.003601	0.006302	0.003241	0.006702	0.007169	0.005092	0.004628	0.002253	0.004857	0.005340
ZnO	0.019131	0.037400	0.022520	0.039557	0.020223	0.042046	0.044871	0.031853	0.029032	0.014052	0.030399	0.033421
ZrO_2	0.010665	0.023699	0.020563	0.011195	0.007150	0.017818	0.026846	0.026820	0.018125	0.008153	0.007721	0.008263

METHODS

The IGCM was used in geochemical calculations to model aqueous concentrations of dissolved glass components in static dissolution tests performed with the 24 eLAW glasses and reported by Crum et al. (2022) and Neeway et al. (2023b). IGCM parameters were varied to optimize

agreement with the measured aqueous concentrations of B, Na, and Si as a function of time and thus determine the best-fit model parameters for this series of static dissolution tests. This section describes the IGCM, the approach used to perform the geochemical calculations, the parameters of the IGCM, and the procedure followed to fit the static dissolution test data.

ILAW glass corrosion model. The IGCM used in this work is composed of four distinct but coupled processes:

1. *Glass dissolution:* this process is modeled by the following dissolution rate equation, which describes the glass dissolution rate, r_{diss}, as a function of distance from pseudo-equilibrium:

$$r_{\text{diss}} = k_0 a_{\text{H}^+}^{-\eta} \exp\left(\frac{-E_a}{RT}\right)\left[1 - \left(\frac{Q}{K_g}\right)^{\sigma}\right] \qquad \text{Eq. 1}$$

where r_{diss} is the glass dissolution rate (mol_{glass} m^{-2} s^{-1}), k_0 is the intrinsic rate constant (mol_{glass} m^{-2} s^{-1}), a_{H+} is the hydrogen ion activity (unitless), η is the pH power law coefficient (unitless), E_a is the activation energy (J mol^{-1}), R is the ideal gas constant (8.314 J K^{-1} mol^{-1}), T is the temperature (K), Q is the ion activity product for glass (unitless), K_g is the pseudo-equilibrium constant for glass (unitless), and σ is the Temkin coefficient (unitless). Because the glass dissolution reaction has no back-reaction (glass does not form in aqueous solution), r_{diss} in Eq. 1 is zero if $Q \geq K_g$. The glass pseudo-equilibrium is assumed to be controlled by the activity of orthosilicic acid (i.e., $Q = a_{H_4SiO_4}$). When $Q << K_g$ the glass dissolves at the forward rate (Stage I). The Temkin coefficient is assumed to be 1 (Lasaga 1995).

2. *Ion exchange:* this process is modeled by a constant (Eq. 7), time-dependent (Eq. 8), or time- and pH-dependent rate of ion exchange (Eq. 9), r_{IEX}, between hydronium ions in solution and sodium ions within the glass matrix. The ion-exchange reaction is defined as:

$$\text{Glass–Na}_{(s)} + \text{H}^+_{(aq)} \rightarrow \text{Glass–H}_{(s)} + \text{Na}^+_{(aq)} \qquad \text{Eq. 2}$$

where Glass–$Na_{(s)}$ represents the pristine glass containing Na and Glass–$H_{(s)}$ represents the hydrated glass where Na has been replaced with an equimolar amount of H. The hydrated glass dissolves according to the same glass dissolution rate equation and with the same parameters as the pristine glass (Eq. 1). Though a similar reaction can occur with other alkali ions (e.g., Li^+ and K^+), Na^+ comprises almost all the alkali content of the eLAW glasses (the Na_2O mole fraction varies from 0.159 to 0.217, the K_2O mole fraction varies from 0.004 to 0.014, and Li_2O is not present, Table 1). Thus, considering Na^+ is sufficient to adequately represents the ion-exchange reaction.

3. *Secondary phase formation and elemental retention in glass alteration layers:* this process is modeled by a set of twelve equilibrium phases, referred to as the incongruent dissolution representation (IDR): analcime ($Na_{0.96}Al_{0.96}Si_{2.04}O_6 \cdot H_2O$), anatase ($TiO_2$), baddeleyite ($ZrO_2$), calcite ($CaCO_3$), chalcedony ($SiO_2$), amorphous iron(III) hydroxide ($Fe(OH)_3$), gibbsite ($Al(OH)_3$), sepiolite ($Mg_4Si_6O_{15}(OH)_2 \cdot 6H_2O$), γ-zinc hydroxide ($Zn(OH)_2$), K-analcime ($K_{0.96}Al_{0.96}Si_{2.04}O_6 \cdot H_2O$), Li-analcime ($Li_{0.96}Al_{0.96}Si_{2.04}O_6 \cdot H_2O$), and cassiterite ($SnO_2$). These phases were selected, and their equilibrium constants parameterized, using a set of nuclear waste glass static dissolution test data (Neeway et al. 2023a).
4. *Aqueous speciation of dissolved glass components:* this process is modeled using a thermodynamic database of equilibrium constants. The thermodynamic database 'thermo.com.V8.R6.230' (Johnson et al. 2000) is used for the equilibrium constants of all aqueous species.

Geochemical calculations. The geochemical calculation software PHREEQC (PH-REdox-EQuilibrium in C) (Parkhurst and Appelo 2013) was employed to model the corrosion of the 24 eLAW glasses in static dissolution tests. The geochemical calculations reproduced the conditions

of the static dissolution tests reported by Crum et al. (2022) and Neeway et al. (2023b). The temperature was 90 °C or 40 °C. The solution volume was 75 mL and the initial glass mass was 7.5 g to achieve a glass-surface-area-to-solution-volume ratio of approximately 2000 m^{-1} based on a specific surface area of approximately 0.02 $m^2\ g^{-1}$ (Crum et al. 2022). The initial solution used in the simulations was generated by equilibrating pure water with atmospheric CO_2 ($P_{CO_2} = 39$ Pa) and O_2 ($P_{O_2} = 20\ k$Pa) at the temperature of interest. The glass dissolution reaction was then modeled in the absence of CO_2 and O_2, i.e., assuming the reaction took place in a fully hermetic vessel with no headspace. All the calculations were run to 720 days (longest static dissolution tests at 40 °C and 90 °C were 700.1-day and 703.7-day long, respectively). A logarithmic-based integration timestep (10×10^{-6} d, 9×10^{-5} d, 9×10^{-4} d, 9×10^{-3} d, 9×10^{-2} d, 9×10^{-1} d, and 719×10^{0} d) was used in the calculations. The compositions of the 24 eLAW glasses (Table 1) were those reported by Crum et al. (2021) and Neeway et al. (2023b). The 24 eLAW glasses are referred to as eLAW-01 through eLAW-24 (the notation without a dash is equivalent). For the glass compositions used in the calculations, halogens were normalized out and the mass fraction of SO_3 in each glass was the target value or predicted solubility limit, whichever was lower (Crum et al. 2022).

To capture the IEX reaction in the geochemical models, the hydrated glass (Glass–$H_{(s)}$) is created by substituting H^+ for Na^+ in the pristine glass (Glass–$Na_{(s)}$), and the dissolution rates in mol s^{-1} of the pristine glass and hydrated glass, denoted by r_p and r_h, respectively, are defined as:

$$r_p = A_p r_{diss} + A_p r_{IEX} \quad \text{Eq. 3}$$

and

$$r_h = A_h r_{diss} - A_p r_{IEX} \quad \text{Eq. 4}$$

where r_{diss} is defined in Eq. 1 and A_p and A_h (m^2) are the surface areas of the pristine glass and hydrated glass, respectively, and are defined as:

$$A_p = SSA \times n_p \times MW_p \quad \text{Eq. 5}$$

and

$$A_h = SSA \times n_h \times MW_h \quad \text{Eq. 6}$$

where SSA ($m^2\ g^{-1}$) is the glass specific surface area (assumed to be the same for the pristine glass and hydrated glass), n_p and n_h (mol_{glass}) are the number of moles of pristine glass and hydrated glass (n_h is zero at the start of each calculation), respectively, and MW_p and MW_h ($g_{glass}\ mol_{glass}^{-1}$) are the molecular weights of the pristine glass and hydrated glass, respectively. Three equations to define the IEX rate, r_{IEX} ($mol_{glass}\ m^{-2}\ s^{-1}$), were considered in this work:

$$r_{IEX} = k_2^T \quad \text{Eq. 7}$$

$$r_{IEX} = k_3^T \times \frac{1}{t^p} \quad \text{Eq. 8}$$

and

$$r_{IEX} = k_4^T \times \frac{1}{t^p} \times 10^{-\alpha \times pH} \quad \text{Eq. 9}$$

where k_2^T ($mol_{glass}\ m^{-2}\ s^{-1}$), k_3^T ($mol_{glass}\ m^{-2}\ s^{p-1}$), and k_4^T ($mol_{glass}\ m^{-2}\ s^{p-1}$) are empirical rate constants at temperature T in the 2-, 3-, and 4-parameter fits (see description below), respectively, t is time (s), p is the time power coefficient (unitless), and α is the IEX pH power coefficient (unitless).

IGCM parameters. The molecular weights (*MW*) of the pristine glass (Eq. 5) and hydrated glass (Eq. 6) were those calculated using the atomic weights listed in the thermodynamic database 'thermo.com.V8.R6.230'. The specific surface areas (*SSA* in Eq. 5 and Eq. 6) were those reported in Crum et al. (2022) and listed in Table 2. The forward-rate model parameters (η, E_a,

and k_0 in Eq. 1, Table 2) were those derived from stirred-reactor coupon analysis (SRCA) (ASTM C1926-23, 2023) and reported by Ryan et al. (2021).

Table 2. Molecular weights, specific surface areas, and forward-rate model parameters of the 24 eLAW glasses.

Glass	MW_p (g mol^{-1})	MW_h (g mol^{-1})	SSA (m^2 g^{-1})	k_0 (mol$_{glass}$ m^{-2} s^{-1})	η (unitless)	E_a (kJ mol^{-1})
eLAW-01	69.141	57.510	0.01976	399.615	0.64	100.57
eLAW-02	66.626	55.048	0.02021	16941.229	0.19	78.01
eLAW-03	66.191	59.119	0.02015	31080.567	0.20	83.78
eLAW-04	69.464	59.887	0.01945	449.059	0.43	86.90
eLAW-05	67.921	58.045	0.02042	6078.259	0.26	82.34
eLAW-06	68.983	59.981	0.02049	1860.561	0.65	104.68
eLAW-07	67.337	59.918	0.01954	1415.284	0.56	99.16
eLAW-08	67.282	55.295	0.01974	963.958	0.59	100.44
eLAW-09	68.381	60.201	0.02052	1977.206	0.52	94.82
eLAW-10	67.595	60.046	0.02012	36205.304	0.15	77.05
eLAW-11	66.330	57.205	0.02021	301.730	0.62	97.84
eLAW-12	67.922	59.288	0.02027	252.583	0.63	97.82
eLAW-13	67.953	60.455	0.01956	5993.492	0.55	101.73
eLAW-14	69.514	58.765	0.01945	656.637	0.63	100.61
eLAW-15	66.799	55.663	0.01935	404.812	0.80	109.99
eLAW-16	67.784	59.721	0.02038	79.020	0.62	95.20
eLAW-17	65.353	56.215	0.01997	189.531	0.77	106.99
eLAW-18	68.588	57.591	0.01998	128.886	0.53	88.04
eLAW-19	70.010	62.031	0.01958	2066.452	0.56	100.21
eLAW-20	67.553	55.909	0.02002	590.109	0.61	100.89
eLAW-21	68.742	59.024	0.01983	2438.178	0.60	103.47
eLAW-22	66.507	55.802	0.02034	403.672	0.79	110.17
eLAW-23	68.860	56.704	0.01982	80.091	0.77	101.93
eLAW-24	67.959	59.211	0.01954	41.422	0.47	81.44

The simulations used the IDR reported by Neeway et al. (2023a). The solid phases in the IDR and their equilibrium constants are listed in Table 3. The IEX rate model parameters (Eq. 7 through Eq. 9) and K_g (Eq. 1) were used as free parameters of the fits.

Table 3. Equilibrium constants at 40 °C and 90 °C of the solid phases in the incongruent dissolution representation.

Solid phase	Chemical formula	log K at 90 °C	log K at 40 °C
Analcime	$Na_{0.96}Al_{0.96}Si_{2.04}O_6 \cdot H_2O$	6.38	8.46
Anatase	TiO_2	−4.80	−5.54
Baddeleyite	ZrO_2	−3.70	−3.87
Calcite	$CaCO_3$	1.20	1.50
Chalcedony	SiO_2	−2.63	−3.17
Iron hydroxide	$Fe(OH)_3$	7.40	7.00
Gibbsite	$Al(OH)_3$	4.46	8.80
Sepiolite	$Mg_4Si_6O_{15}(OH)_2 \cdot 6H_2O$	38.00	42.37
γ-zinc hydroxide	$Zn(OH)_2$	11.70	11.70
K-analcime	$K_{0.96}Al_{0.96}Si_{2.04}O_6 \cdot H_2O$	4.90	6.98
Li-analcime	$Li_{0.96}Al_{0.96}Si_{2.04}O_6 \cdot H_2O$	5.90	7.98
Cassiterite	SnO_2	−35.35	−41.87

Fitting approach. Three sets of parameter optimizations (or fits) were performed: 2-parameter fits in which the constant IEX rate model term was used and the fitting parameters were K_g and the IEX empirical rate constant (k_2^T); 3-parameter fits in which the time-dependent IEX rate model term was used and the fitting parameters were K_g, k_3^T, and the time power coefficient (p); 4-parameter fits in which the time- and pH-dependent IEX rate model term was used and the fitting parameters were K_g, k_4^T, p, and the IEX pH power coefficient (α). A two-step fitting approach was employed for each of the three sets of fits.

In the first step, a wide range of parameter values was considered using a coarse parameter grid. The model parameters used in the coarse parameter grid for the three sets of fits were as follows. At 40 °C, log K_g was varied from −4.6 to −3.0 and, at 90 °C, from −4.2 to −2.6 in 0.2 intervals at both temperatures. In the 2-parameter fits, k_2^T was varied in 0.2 intervals from −13.6 to −8.8 at 40 °C and from −12.8 to −8.0 at 90 °C. In the 3- and 4-parameter fits, $k_{3/4}^T$ was varied

in 0.5 intervals from −12.0 to −3.5 at 40 °C and from −11.0 to −2.5 at 90 °C. The parameters p and α were varied from 0.1 to 0.9 in 0.2 intervals and from 0.05 to 0.25 in 0.05 intervals, respectively. A geochemical calculation was performed for each combination of fitting parameters.

The agreement between predicted and measured concentrations for element X was quantified using the root mean square logarithmic error ($RMSLE_X$), which is defined as:

$$RMSLE_X = \sqrt{\frac{1}{N}\sum_{i=1}^{N}\left(\log_{10} C_{\mathrm{p}} - \log_{10} C_{\mathrm{m}}\right)^2} \qquad \text{Eq. 10}$$

where N is the number of data points, and C_{m} and C_{p} are the measured and predicted concentrations of the element of interest at a given solution sampling. Contour plots of the RMSLE of key elements at all $\log K_{\mathrm{g}}$ and $k^T_{2/3/4}$ values and for key values of p and α are generated for each fit-glass-temperature combination. The complete set of contour plots is reported in Section A of the Supporting Information (SI) document. For each glass, at each temperature, the best fit was defined as the combination of fitting parameters that minimized ($RMSLE_B$ + $RMSLE_{Na}$ + $RMSLE_{Si}$)/3, which will be referred to as the goodness-of-fit statistics.

In the second step, a finer grid of parameter values centered around the best-fit parameters from the coarse grid was considered. The model parameters used in this second step were as follows: $\log K_{\mathrm{g}}$, $k^T_{2/3/4}$, p, and α were varied about the minimum identified with the coarse grid by −0.2 to +0.2 in 0.01 intervals, by −0.5 to +0.5 in 0.05 intervals, by −0.1 to +0.1 in 0.02 intervals, and by −0.03 to +0.03 in 0.01 intervals, respectively. Similar to the first step, a geochemical calculation was performed for each combination of parameters and the best-fit parameters from the fine grid were determined based on the goodness-of-fit statistics. In both

steps, the p value and the p-α pair of values for the 3- and 4-parameters fits, respectively, that minimized the average of the goodness-of-fit statistics at 40 °C and 90 °C were selected as the best-fit parameters for each glass. This calculation was needed because p and α are temperature-independent parameters and performing fits independently at the two temperatures may result in different optimized values of p and α at the two temperatures for a given glass.

In preliminary calculations, the model predicted, in a few cases, a sudden, step-like increase in the calculated B and Na concentrations and a commensurate decrease in the calculated Si concentration. These changes in predicted concentrations coincided with the rapid and extensive growth of analcime once saturation with respect to this phase was achieved. An approach was therefore developed to remove those model parameter sets. The occurrence of such a step increase of the predicted dissolved glass component concentrations was detected by calculating the second derivative of the predicted B concentration with respect to time and removing the model parameter sets that led to fluctuations greater than a cutoff value. The second derivative of the predicted B concentration at time i, $C_B''(i)$, was calculated using a second-order forward finite difference:

$$C_B''(i) = \frac{C_B(i+1) - 2 \times C_B(i) + C_B(i-1)}{h^2} \qquad \text{Eq. 11}$$

where h is $\big(t(i+1) - t(i-1)\big)/2$ and $t(i)$ is time at time point i. A set of model parameters that led to the difference between the maximum and minimum values of $C_B''(i)$ being greater than a cutoff value of 0.1 mg L^{-1} d^{-2} after t = 10 days was ignored for the purposes of determining the best-fit model parameter values and was assigned a RMSLE of 1 for the purposes of generating contour plots.

RESULTS

Analysis of parameter space and fitting results. The top panel of Figure 1 shows an example (eLAW-01, 40 °C) of a set of contour plots of the RMSLEs of B, Na, and Si as a function of log K_g and log r_{IEX} generated using the 225 calculations performed for the 2-parameter fit with the coarse parameter grid. The results are exemplative of the general trends observed with other glasses (see Section A of the SI). The correlation between log K_g and log k_2^T is apparent in the B, Na, and Si RMSLE contour plots. As log K_g increases, the value of log k_2^T needed to optimize the agreement with experimental data decreases. To understand this finding, we first need to understand how K_g and r_{IEX} (=k_2^T in the 2-parameter fits) individually affect the extent of glass dissolution. Without the IEX reaction, the glass would dissolve until the activity of orthosilicic acid reaches K_g, at which point the glass dissolution reaction would stop and the concentrations of dissolved B, Na, and Si would remain constant. When the IEX reaction is included in the IGCM, Na^+ ions are continuously released into solution, which raises the solution pH, decreases the activity of orthosilicic acid (first pK_a at 25 °C is 9.8), preventing it from reaching K_g, which, in turn, keeps the glass dissolution reaction going. Therefore, the extent of glass dissolution, as determined by the concentrations of dissolved B, Na, and Si, is positively correlated to both K_g and r_{IEX} (the calculated concentrations of B, Na, and Si, in this case, increase as both K_g and r_{IEX} increase). This means that, for a given extent of glass dissolution, increasing K_g would decrease the value of r_{IEX} needed to optimize agreement with experiment, and, similarly, increasing r_{IEX} would decrease the value of K_g needed to optimize agreement with experiment. In other words, K_g and r_{IEX} are negatively correlated in the fits.

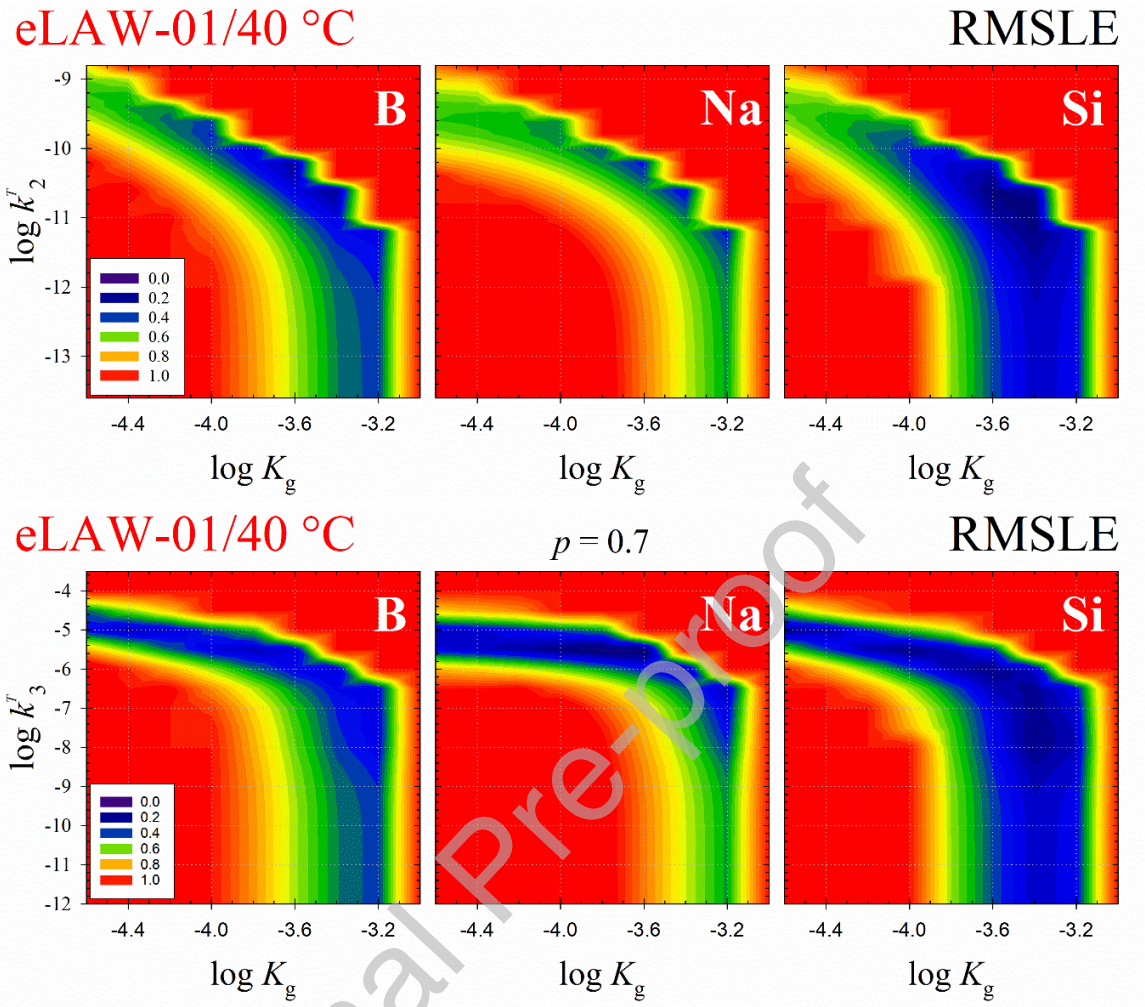

Figure 1. 2-parameter (top) and 3-parameter (bottom) fits, eLAW-01, 40 °C, coarse parameter grid. Contour maps of the B, Na, and Si RMSLEs as a function of log $k^T_{2/3}$ and log K_g. Color ranges from purple (low RMSLE) to red (high RMSLE).

For the highest values of K_g, two important phenomena emerge. First, the negative correlation between r_{IEX} and K_g disappears. To understand this phenomenon, recall that the extent of glass dissolution, as determined by the concentrations of dissolved B, Na, and Si, is correlated to both K_g and r_{IEX}. This means that, if K_g is such that the predicted values of the dissolved B, Na, and Si concentrations at pseudo-equilibrium and without the IEX reaction would be higher than the

measured values, then there is no (positive) value of r_{IEX} that would improve agreement with the measured concentrations. Second, the RMSLEs of B, Na, and Si suddenly and rapidly increase as log K_g increases beyond approximately −3.2 in the example of a fit at 40 °C shown in the top panel of Figure 1. This phenomenon is the result of log K_g reaching and surpassing the log K of chalcedony used in the IGCM (−3.17 at 40 °C, Table 3). The ion activity product of glass and that of chalcedony are the same, i.e., $Q = a(H_4SiO_4)$ for both glass (Eq. 1) and chalcedony ($SiO_2 + 2\ H_2O \leftrightarrow H_4SiO_4$). Consequently, in practical terms regarding modeling glass corrosion with the current formulation of the IGCM, log K_g cannot exceed the log K of chalcedony. If log K_g exceeds the log K of chalcedony, the formation of chalcedony fixes the activity of orthosilicic acid below the value of K_g, which, in turn, fixes the chemical affinity term of the glass dissolution equation to below 1 and rapidly drives the glass dissolution reaction to completion.

Another phenomenon emerges at high values of log k_2^T that results in step-like features in the RMSLE contour plots. These step-like features at the upper log k_2^T end of the RMSLE valley for a given value of log K_g arise because, as detailed above, sets of model parameters that lead to a step increase in the calculated concentration of B are removed from consideration and are given a RMSLE value of 1 for the purposes of generating the contour plots. The step increase in the calculated concentration of B in these cases is correlated to the growth of analcime ($Na_{0.96}Al_{0.96}Si_{2.04}O_6 \cdot H_2O$) (Table 3). If r_{IEX} and therefore the Na release are high and the concentration of dissolved Al is not limiting, analcime growth can be significant enough to reduce the chemical affinity term and thus drive rapid glass dissolution. This phenomenon was not observed in the static dissolution tests (Crum et al. 2022; Neeway et al. 2023b), and the approach of removing step increases in the calculated concentration of B was therefore

implemented to remove from consideration the sets of model parameters that led to this phenomenon.

Using the same glass (eLAW-01) and temperature (40 °C) as for the 2-parameter fit shown in the top panel of Figure 1, the bottom panel of Figure 1 shows an example of a set of B, Na, and Si RMSLE contour plots obtained from the 810 combinations of fitting parameters of the coarse parameter grid used in the 3-parameter fits (i.e., when the time-dependent term, p, is introduced). Each plot provided in the bottom panel of Figure 1 shows the results at a value of p of 0.7. The general shape of the contour plots is the same as that of the contour plots obtained from the 2-parameter fits, with an obvious correlation between log K_g and log k_3^T. Specifically, an abrupt increase of the RMSLE occurs when log K_g equals log K of chalcedony, and less pronounced, but still present, step-like features at high log k_3^T are observed. The correlation between log K_g and log k_3^T shifts to higher values of log k_3^T for a given value of log K_g as the parameter p is introduced. Higher values of p mean a more rapid decrease of the magnitude of the IEX reaction with time, so an increasing value of log k_3^T is needed to optimize agreement between predicted and measured concentrations with increasing p values. Numerical convergence issues with the geochemical calculations may arise as p approaches 0.9 (i.e., the highest considered value of p). In Eq. 8 and Eq. 9, the limit of k_3^T is infinity as t tends to zero, which can cause numerical convergence problems for the initial time steps, especially for high values of p.

Using the same glass (eLAW-01) and temperature (40 °C) as for the examples of the 2- and 3-parameter fits, the top panel of Figure 2 shows an example of a set of B, Na, and Si RMSLE contour plots obtained from the 4050 combinations of fitting parameters in the 4-parameter fits (i.e., when the pH-dependent term, α, is introduced). Again, the general shape of the contour plots is the same as that of the contour plots obtained from the 2- and 3-parameter fits, with an

obvious correlation between log K_g and log k_4^T, an abrupt increase of the RMSLE when log K_g equals log K of chalcedony, and step-like features at high log k_4^T. The correlation between log K_g and log k_4^T shifts to higher values of log k_4^T for a given value of log K_g as p remains constant and α is introduced. Because the pH of the aqueous solution in the modeled static dissolution tests generally increases with time, higher values of α mean a more rapid decrease of the magnitude of the IEX reaction with time, so that an increasing value of log k_4^T is needed to optimize agreement between predicted and measured concentrations.

The minimum RMSLE is also plotted as a function of p and α for B, Na, and Si in the bottom panel of Figure 2. These results show that, while a value of p often clearly minimizes the RMSLE, a range of values of α often yield similar RMSLEs for a given value of p. This is because, after a short initial period of rapid pH increase, the pH of the aqueous solution increases slowly with time, which makes isolating and parameterizing the effect of pH from this dataset difficult.

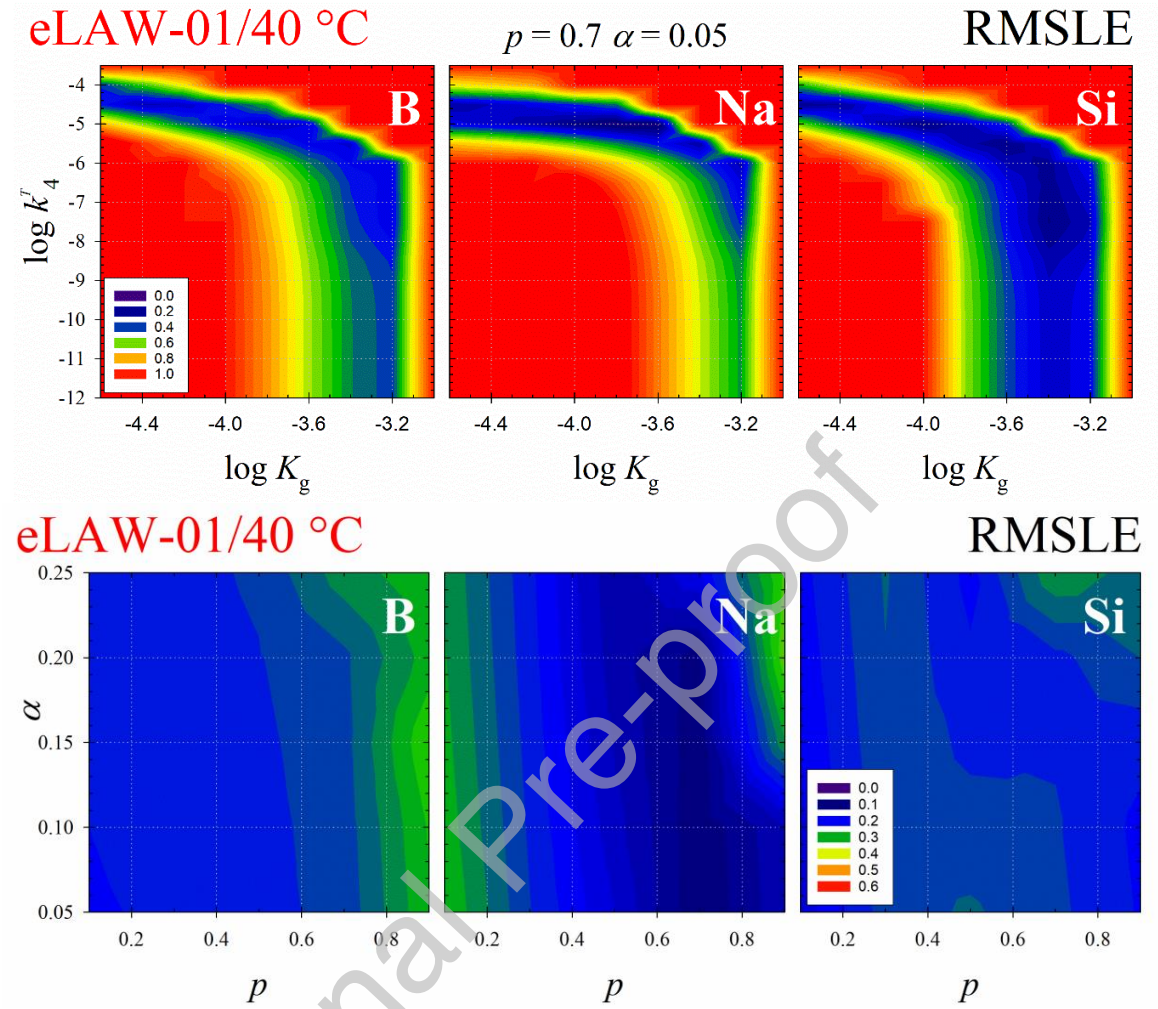

Figure 2. 4-parameter fit, eLAW-01, 40 °C, coarse parameter grid. Contour maps of the B, Na, and Si RMSLEs as a function of log k_4^T and log K_g (top) or α and p (bottom). Color ranges from purple (low RMSLE) to red (high RMSLE).

Section B of the SI shows contour plots of the goodness-of-fit statistics (i.e., average of the B, Na, and Si RMSLEs) obtained from the 2-, 3-, and 4-parameter fits performed at 40 °C and 90 °C with the coarse and fine parameter grids. An example (2-parameter fit at 40 °C) is shown in Figure 3. Each figure in Section B of the SI as well as the example in Figure 3 display contour plots for half of the 24 eLAW glasses for a fit type-temperature combination and is divided into

an upper part showing the results obtained with the coarse parameter grid and a lower part showing the results of the fine grid. White dots indicate the position of the minimum of the goodness-of-fit statistics in each panel. Recall that the fine grid is centered around the minimum of the goodness-of-fit statistics determined with the coarse grid. The axes of the contour plots generated with the fine grid are therefore labeled as $\Delta\log K_g$ and $\Delta\log k^T_{2/3/4}$ where Δ indicates that the displayed values are relative to those corresponding to the goodness-of-fit minimum obtained with the coarse grid (white dots in the panels in the upper part of the figure). For the 3- and 4-parameter fits, the values of p and of p and α, respectively, are shown in each panel. The contour plots of the goodness-of-fit statistics obtained with the coarse parameter grid show the same features as discussed for the B, Na, and Si RMSLEs in the examples used previously in this section.

The contour plots of the goodness-of-fit statistics obtained with the fine parameter grid show three main types of minima. The first type, as exemplified by eLAW-07 in Figure 3, is when the minimum is located at the bottom of a clear and well-defined basin. In these cases, the best fit is expected to not be dependent on small changes in the parameter values or experimental uncertainties. The second type, as exemplified by eLAW-04 in Figure 3, is when the minimum is also located at the bottom of a clear basin, but this basin is truncated by the presence of a sharp boundary such as that caused by the $\log K$ of chalcedony. Here, small changes in the best-fit parameter values may have significant effect on the IGCM predictions, if those changes cause the goodness-of-fit statistics to cross the boundary. The third type, as exemplified by eLAW-05 in Figure 3, is when the minimum is not located in a clear basin. In these cases, small changes in the best-fit parameter values in any direction may greatly affect the predictions of the IGCM.

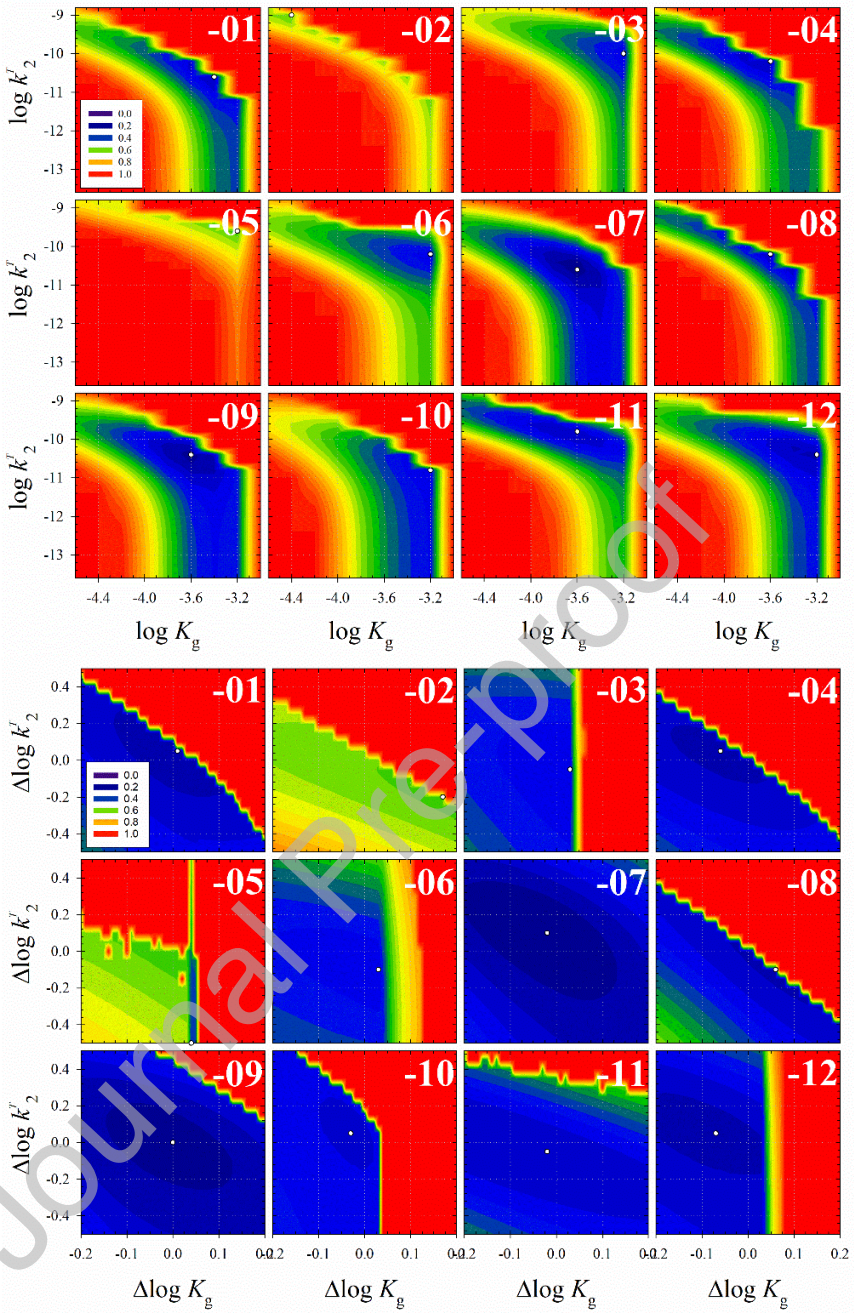

Figure 3. Contour plots of the goodness-of-fit statistics from the 2-parameter fits performed at 40 °C with the coarse (top) and fine (bottom) parameter grids for eLAW-01 through eLAW-12. Δ indicates that the displayed values are relative to the goodness-of-fit minimum obtained with

the coarse grid. The white dots indicate the minimum RMSLE in each panel.

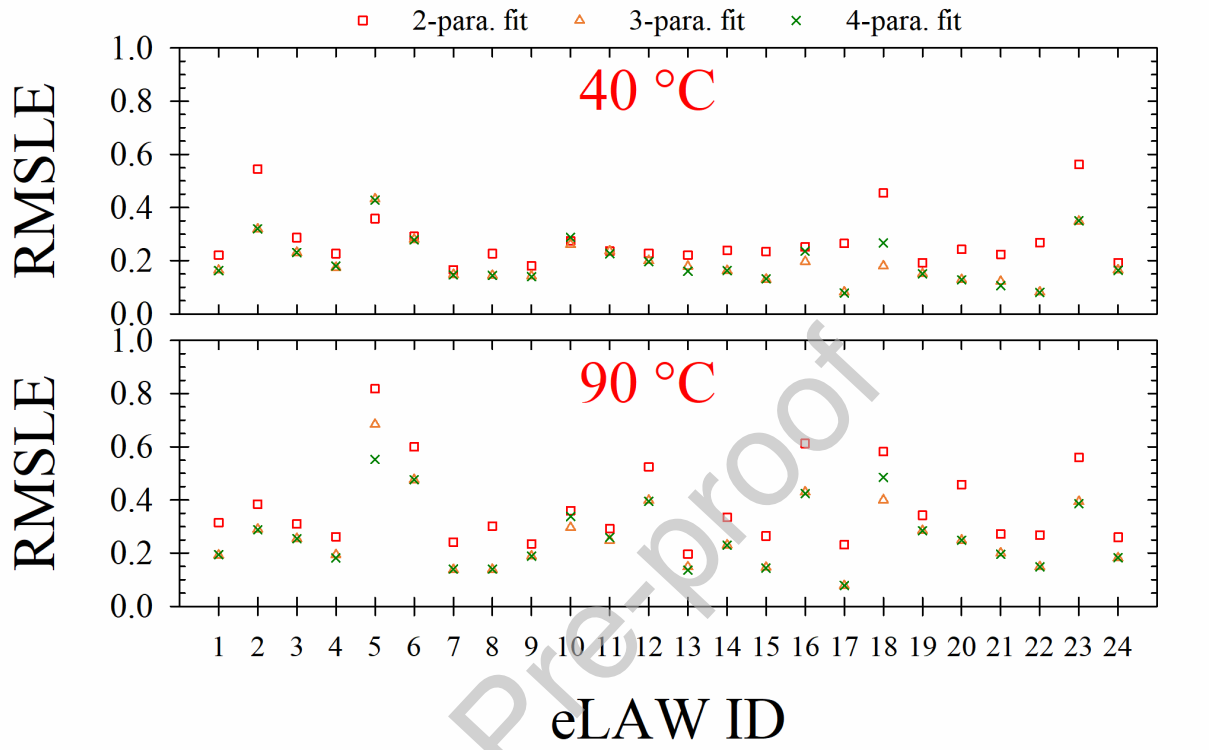

Figure 4. Goodness-of-fit statistics (i.e., average of the B, Na, and Si RMSLEs) for each of the 24 eLAW glasses as obtained from the best 2-, 3-, and 4-parameter fits at 40 °C (top) and 90 °C (bottom).

Figure 4 summarizes the minimum goodness-of-fit statistics obtained for each glass at 40 °C and 90 °C. For both temperatures, the RMSLE decreases significantly when going from the 2-parameter fit to the 3-parameter fit. This finding indicates that the introduction of the time-dependent term systematically improves the agreement between calculated and measured concentrations. In contrast, the change in the RMSLE is small to negligible when going from the 3-paramater fit (i.e., time-dependent) to the 4-parameter fit (i.e., time- and pH-dependent). Again, the change in pH at long times in the static dissolution tests is too small to fully capture

the effect of the parameter α. Additional tests with controlled pH would be necessary to determine the impact of α across a wider range of pH values.

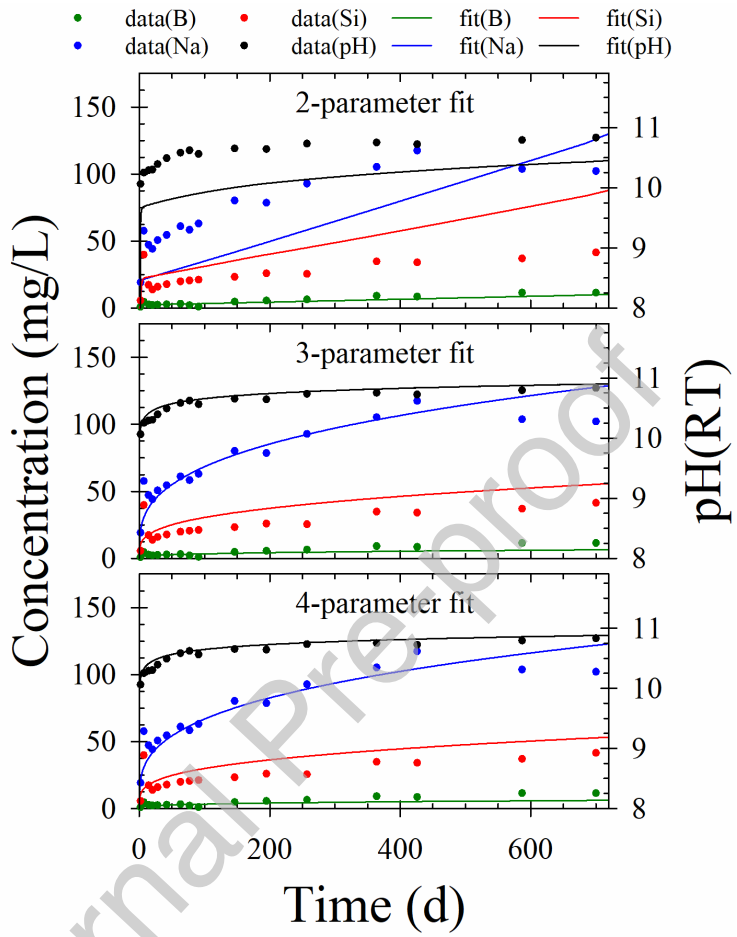

Figure 5. Best fits for eLAW-01 at 40 °C. Measured and calculated concentrations of B, Na, and Si and pH as a function of time from 2- (top), 3- (middle), and 4- (bottom) parameter fits.

Best fits to static dissolution test data. The complete set of best fits obtained with the fine parameter grid for the 24 eLAW glasses at 90 °C and 40 °C is reported in **Error! Reference source not found.**Section C of the SI. An example of a set of 2-, 3-, and 4-parameter best fits with comparison to measured B, Na, and Si concentrations along with pH values as a function of time is shown in Figure 5 for eLAW-01 at 40 °C. Similar trends were observed for other glasses.

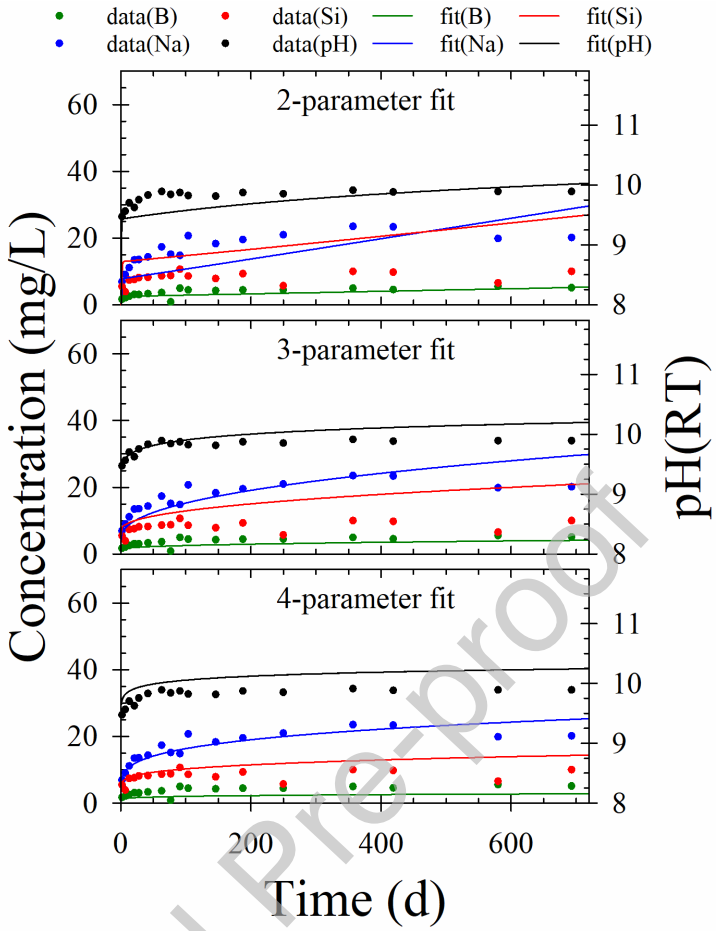

Figure 6. Best fits for eLAW-13 at 40 °C. Measured and calculated concentrations of B, Na, and Si and pH as a function of time from 2- (top), 3- (middle), and 4- (bottom) parameter fits.

The 2-parameter fit uses a constant IEX rate. As a result, after an initial rapid increase of the Na concentration, the predicted release of Na is approximately linear with time (top panel of Figure 5), unlike the measured Na concentrations, which appear to 'roll over'. The 3-parameter best fit shows that the introduction of a time-dependent IEX term can capture the general behavior of the measured concentrations (middle panel of Figure 5), and the goodness-of-fit agreement with experiment is improved (Figure 4). In contrast, the 4-parameter best fit shows that the introduction of a pH-dependent IEX term generally has a minor effect on the predicted concentrations compared to the 3-parameter fit (bottom panel of Figure 5), and the goodness-of-

fit agreement with experiment is essentially unchanged (Figure 4). It is noteworthy and encouraging that the agreement between calculated and measured pH values is good for the 3- and 4-parameter fits, even though pH was not part of the goodness-of-fit statistics.

While the introduction of a pH-dependent IEX term generally has a minor effect on the goodness of fit, there are a few notable exceptions. Figure 6 shows an example of such a case (eLAW-13 at 40 °C). The 2-parameter fit (top panel of Figure 6) is similar to that just discussed for eLAW-01 at 40 °C, whereby the Na release is approximately linear in time (top panel of Figure 5). The 3-parameter fit (middle panel of Figure 6) better captures the behavior of the measured Na release, but the Si concentration and pH are overestimated and so is the Na concentration for later time points. Upon introduction of the pH-dependent term, the predicted Na and Si concentrations more accurately reproduce the measured values (bottom panel of Figure 6), and the goodness-of-fit statistics decreases noticeably (Figure 4). Because the RMSLE statistics is a logarithmic error, a visually small drop in RMSLE in Figure 4 can translate to a noticeable improvement in the best-fit figure such as in Figure 6.

DISCUSSION

Best-fit IGCM parameters and comparison to other parameterization approaches. The best-fit $\log K_g$ and $\log k^T_{2/3/4}$ parameters at both temperatures are displayed in Figure 7 and Figure 8, respectively, and the best-fit p and α parameters in Figure 9. All best-fit parameters are also tabulated in Section C of the SI.

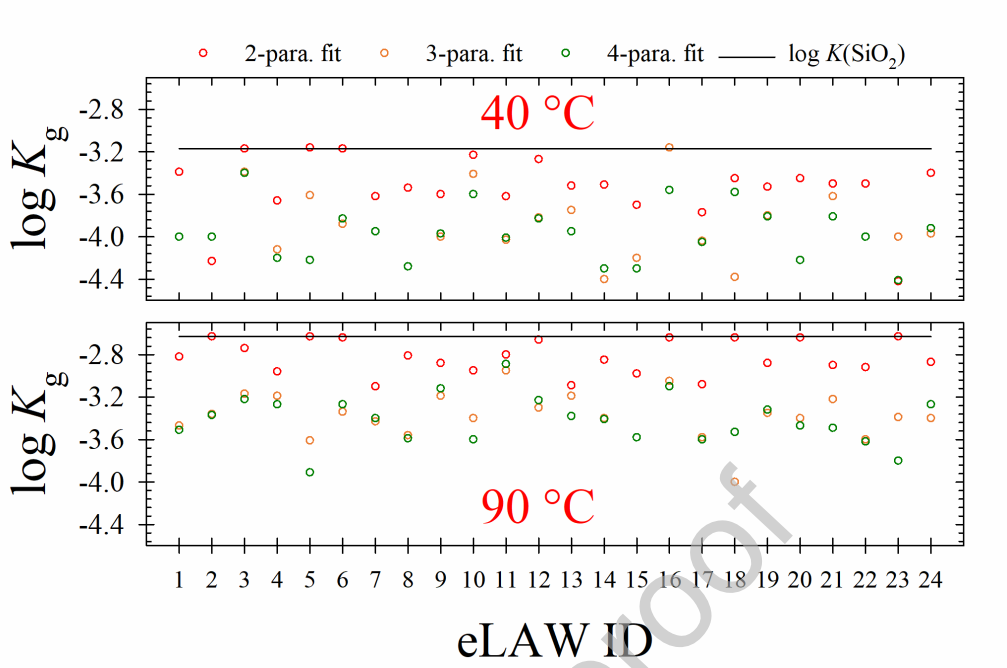

Figure 7. Log K_g of the 24 eLAW glasses from the best 2-, 3-, and 4-parameter fits at 40 °C and 90 °C. The black horizontal line represents the log K of chalcedony.

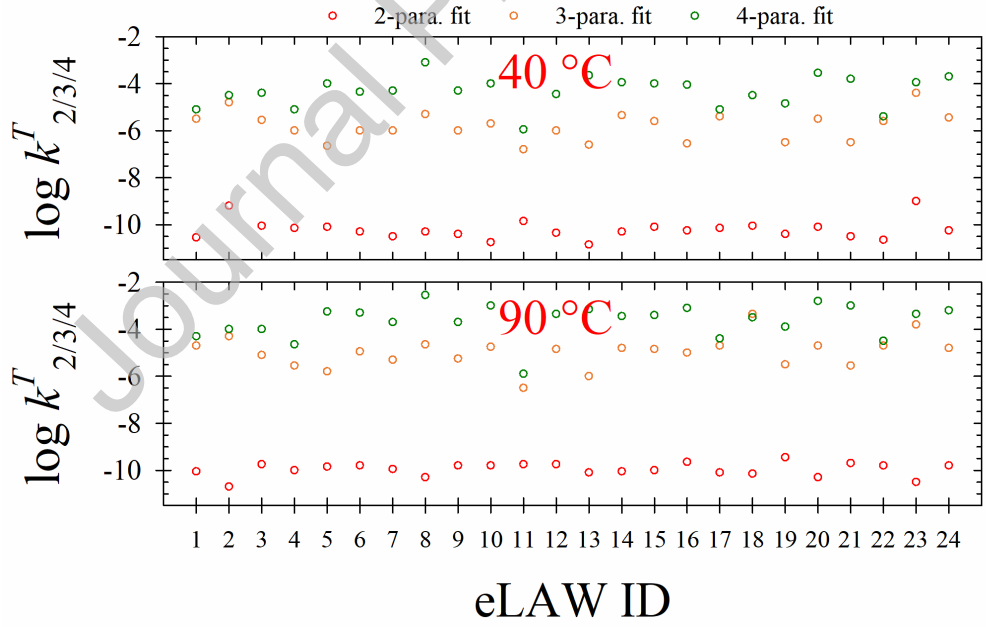

Figure 8. Log $k^T_{2/3/4}$ of the 24 eLAW glasses from the best 2-, 3-, and 4-parameter fits at 40 °C and 90 °C.

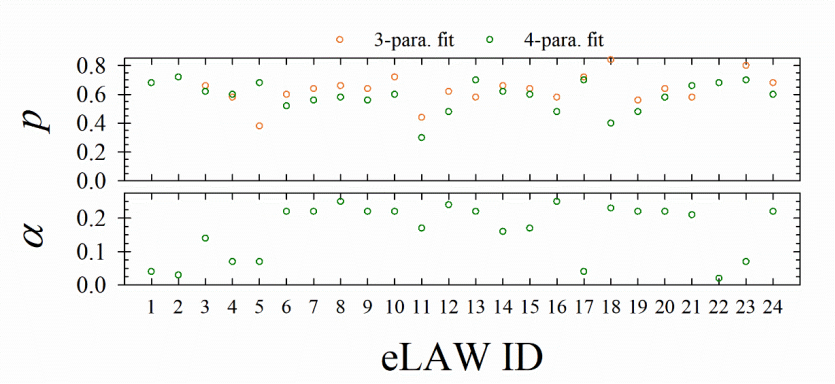

Figure 9. Parameters p and α of the 24 eLAW glasses from the best 3- and 4-parameter fits at 40 °C and 90 °C.

The best-fit log K_g values can be compared to those derived for ILAW glasses from single-pass flow-through (SPFT) tests (Figure 10). Flow-through tests in general and SPFT tests particularly have been used extensively to assess nuclear waste glass durability (Thorpe et al. 2021). Specifically, SPFT tests have been used to parameterize the IGCM in the context of the IDF PA (McGrail et al. 1997; Abraitis et al. 2000a; Abraitis et al. 2000b; Pierce et al. 2004; Neeway et al. 2017; Papathanassiu et al. 2017; Viragh et al. 2017; Neeway et al. 2018a; Viragh et al. 2018). The SPFT approach used to determine K_g, referred to as 'SPFT with Si addition', involves performing a series of SPFT tests at a constant and high flow-rate-to-glass-surface-area (q/S) ratio with different inlet dissolved silica concentrations, and then equating K_g to the x-intercept of a regression of the B normalized loss rate (NLR(B)) as a function of the orthosilicic acid activity. An alternative approach, referred to as 'SPFT q/S', consists in varying the orthosilicic acid activity by performing SPFT tests at multiple q/S ratios—thus varying the activities of all dissolved glass components simultaneously—rather than through Si addition (Kerisit et al. 2021a). The log K_g values obtained in the best fits in this study vary between −3.16 and −4.42 at 40 °C and between −2.63 and −4.00 at 90 °C (Figure 10). In comparison, log K_g values obtained

from SPFT tests with Si addition at pH = 9 (Figure 10) vary between −2.4 and −4.1 at 40 °C and between −1.8 and −3.5 at 90 °C (Kerisit et al. 2021a). At 40 °C, 11 of 16 log K_g values obtained from SPFT tests with Si addition were at or above the log K of chalcedony (−3.17), and, at 90 °C, 8 of 14 values were at or above the log K of chalcedony (−2.63). In comparison, log K_g values obtained from SPFT q/S tests at pH = 9 (Figure 10) vary between −3.6 and −4.5 at 40 °C and between −2.8 and −4.4 at 90 °C (Kerisit et al. 2021a), with none of the values at or above the log K of chalcedony at either temperature.

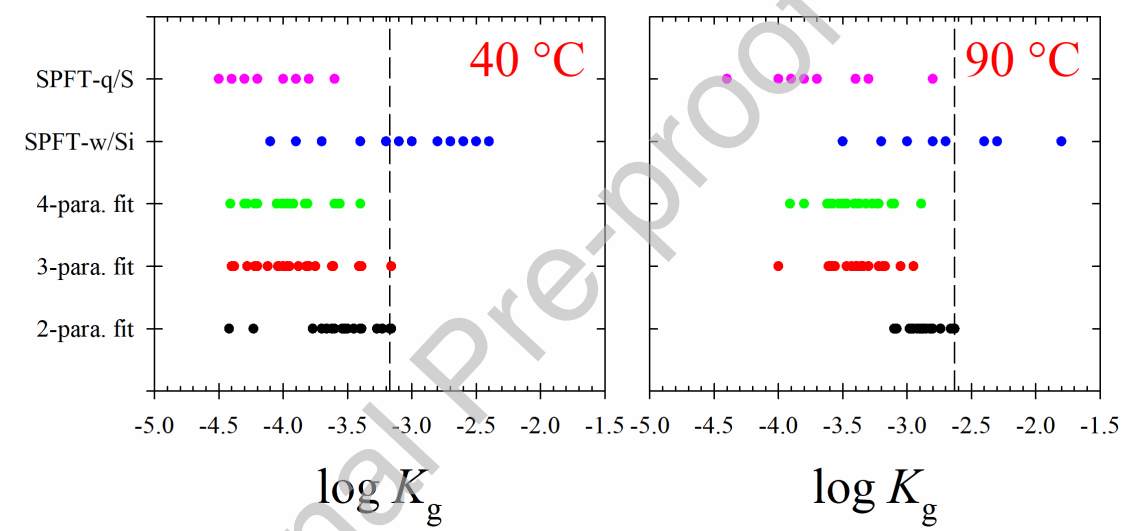

Figure 10. Comparison of log K_g values obtained at 40 °C and 90 °C from 2-parameter fits ("2-para. fit"), 3-parameter fits ("3-para. fit"), 4-parameter fits ("4-para. fit"), SPFT tests with Si addition ("SPFT-w/Si"), and SPFT q/S tests ("SPFT-q/S"). Log K values of chalcedony at the two temperatures are shown as vertical dashed lines.

Overall, the average log K_g values obtained from SPFT q/S tests (−4.1 ± 0.3 at 40 °C and −3.6 ± 0.3 at 90 °C) more closely match those obtained in the 4-parameter best fits (−4.0 ± 0.3 at 40 °C and −3.4 ± 0.3 at 90 °C) than the average log K_g values obtained from SPFT with Si addition (−3.0 ± 0.5 at 40 °C and −2.6 ± 0.5 at 90 °C). This finding is consistent with the

conditions of these tests whereby only the activity of orthosilicic acid is varied in SPFT tests with Si addition whereas the activities of all dissolved glass components change in both SPFT q/S tests and static dissolution tests. Moreover, $\log K_g$ values derived from SPFT tests with Si addition are often higher than the $\log K$ of chalcedony, which is problematic because it drives the glass dissolution to completion, as discussed above.

The $\log k_2^T$ values obtained in the best 2-parameter fits vary between −9.00 and −10.85 at 40 °C and between −9.45 and −10.70 at 90 °C (Figure 8). In comparison, $\log r_{IEX}$ values obtained from SPFT tests with Si addition at pH = 9 vary between −8.8 and −10.2 at 40 °C and between −7.8 and −9.0 at 90 °C (see Kerisit et al. (2021b) and references therein). As already discussed, $\log k_{2/3/4}^T$ values increase significantly when the time-dependent IEX term is introduced, and a smaller further increase of $\log k_{2/3/4}^T$ is calculated when the pH-dependent IEX term is added.

The optimal values of the time power coefficient p vary between 0.38 and 0.84 for the 3-parameter best fits with an average of 0.64 and between 0.30 and 0.72 for the 4-parameter best fits with an average of 0.58 (Figure 9). The decrease of the average p value upon addition of the pH-dependent IEX term is expected since pH increases with time and thus both terms contribute to the decrease of the IEX rate with time. The optimal values of the pH power coefficient α vary between 0.02 and 0.25 with an average of 0.17.

Comparison to parameters from other glass corrosion models. Most glass corrosion models use a first-order chemical affinity term. The original Grambow model (Grambow 1985; Grambow 1987), the Grambow and Müller model (Grambow and Müller 2001), the Techer model (Techer et al. 2000), and the version of the GRAAL model by Rieke et al. (2018) all use a chemical affinity term based solely on the activity of orthosilicic acid, as does the IGCM. Direct

quantitative comparison of K_g values is difficult because these models were not applied to the same glasses as studied in this work and in several instances not at the same temperatures. Nonetheless, Grambow (1985) reported a Si saturation concentration parameter value of 8.25 mg L^{-1} for glass C31-3EC corroded at 90 °C, which translates to a log K_g value of −3.53 and is consistent with the mean values from the 3- and 4-parameter fits (−3.4 ± 0.3 for both). Techer et al. (2000) used a Si solubility of 22 mg L^{-1} for modeling the corrosion of basaltic glass at 90 °C. This value corresponds to a log K_g of −3.11, which is within one standard deviation of the mean values from the 3- and 4-parameter fits. While the study of Rieke et al. (2018) was similar to this work in that it considered a series of glasses with systematic variations in composition, their glass corrosion model used retention factors (whereas the IGCM does not) that ranged from 0.9 to 1.0 for Si but were almost exclusively 0 for B and thus allowed for higher values of log K_g (ranging from −2.82 to −2.30).

Direct comparison of the IEX rate model parameters to other glass corrosion models is not possible because other models do not use the same functional form or do not explicitly model the ion-exchange reaction. In the GRAAL model, for example, the growth of the PRI is a function of its thickness and diffusion coefficient. Notably, the PRI is assumed to grow with the square root of time in the GRAAL model, which would be equivalent to a value of p of 0.5 in the IGCM. This constraint is relaxed in the time-dependent and time- and pH-dependent IEX rate model terms where the average p value for the 24 eLAW glasses is 0.64 ± 0.10 and 0.58 ± 0.10, respectively.

CONCLUSIONS

Geochemical calculations with the ILAW glass corrosion model were used to fit aqueous solution data from static dissolution tests at two temperatures for 24 alkali-borosilicate glasses. This approach allowed quantification of the parameter space over a wide range of IGCM parameter values. The region of parameter space that maximized agreement with experimental data was first identified (coarse parameter grid), and the values of the IGCM parameters were then refined by repeating the approach with a finer parameter grid. The model parameters thus derived expand the glass composition space for which parameters of any glass corrosion model are available. The derived parameters also provide an opportunity to take advantage of the statistical design of the eLAW glass matrix and develop composition–parameter correlation models capable of predicting IGCM parameters such as the IEX rate model parameters, and thus glass corrosion behavior, solely based on glass composition. This general approach could also be easily applied to other available experimental datasets.

The RMSLE contour maps revealed a clear negative correlation between $\log K_g$ and $\log r_{IEX}$. This finding has implications for the execution of sensitivity analyses of selected parameters as part of performance assessments of disposal facilities that utilize both parameter sets; that is, model parameters cannot be varied independently without risking entering an unrealistic region of the parameter space. A similar conclusion was made for the forward rate model parameters (η, E_a, and k_0) (Neeway et al. 2018b; Vienna et al. 2018). The RMSLE contour maps also showed the existence of strict limits on the potential values of $\log K_g$ for simulating static dissolution tests. Specifically, $\log K_g$ cannot be higher than the $\log K$ of chalcedony or the formation of chalcedony will fix the chemical affinity term to less than 1 and drive the glass dissolution reaction to completion. Many $\log K_g$ values, if obtained from SPFT tests with Si addition, are higher than the $\log K$ of chalcedony and are thus expected to lead to large overpredictions of the

extent of glass corrosion. In contrast, log K_g values obtained from SPFT q/S tests are generally lower and thus do not suffer from this problem because they vary the activities of all dissolved glass components simultaneously, highlighting the importance of test conditions when determining glass corrosion model parameters.

The RMSLEs from the best 2- (constant r_{IEX}), 3- (time-dependent), and 4-parameter (time- and pH-dependent) fits together with visual comparison of the predicted and measured B, Na, and Si aqueous concentrations showed a significant improvement of the best fits with the introduction of a time-dependent term (RMLSE decreased by up to 0.28). Addition of a time dependent term is therefore a simple and efficient mean to complement the chemical affinity term in accounting for reaction progress. In contrast, the improvement of the best fits with the introduction of a pH-dependent term was generally small (RMSLE decreased by up to 0.02, except for eLAW-05 at 90 °C). This is a consequence of the measured pH values in these static dissolution tests not varying significantly past a short period of rapid increase. Additional testing in pH-controlled solutions would be required to parameterize the pH-dependence of the IEX reaction more reliably. This finding indicates that multiple glass corrosion tests need to be performed to ensure comprehensive model parameterization if glass corrosion models are to accurately reproduce changes in corrosion behavior with reaction progress and conditions.

Toward this goal of ensuring comprehensive model parameterization, the approach employed in this work could be applied to other types of glass corrosion tests (Thorpe et al. 2021) such as SPFT tests or pressurized unsaturated flow (PUF) tests (Pierce et al. 2006). Because the other types of corrosion tests are performed in different conditions and a robust and versatile glass corrosion model should be applicable to a range of conditions, a comparison of the IGCM

parameters derived from various corrosion tests would help identify and remediate any shortcomings of the IGCM.

ACKNOWLEDGMENTS

This research was supported by Washington River Protection *Solutions*, LLC (WRPS) as part of the ILAW Glass Testing for Disposal at IDF project at Pacific Northwest National Laboratory (PNNL). PNNL is operated for the U.S. Department of Energy (DOE) by Battelle Memorial Institute under Contract DE-AC05-76RL01830. The simulations were performed using PNNL Research Computing and the Environmental Molecular Sciences Laboratory (EMSL), a national scientific user facility sponsored by the U.S. DOE's Office of Biological and Environmental Research and located at PNNL in Richland, WA. The authors acknowledge WRPS team members Rodney S. Skeen, Kearn Patrick Lee, David J. Swanberg, Jeanne K. Bernards, and Ridha Mabrouki for programmatic and technical guidance and support. The authors thank Joelle T. Reiser at PNNL for her review of this manuscript. The authors also thank Ian L. Pegg and co-workers at the Vitreous State Laboratory, Catholic University of America, for useful discussions.

AUTHOR INFORMATION

Corresponding Author

*Phone: (509) 371-6382; e-mail: sebastien.kerisit@pnnl.gov.

SUPPORTING INFORMATION

Compositions of the 24 eLAW glasses; contour maps of parameter space for the 2-, 3-, and 4-parameter fits to static dissolution test data at 40 °C and 90 °C for the 24 eLAW glasses; contour maps of the goodness-of-fit statistics for the 2-, 3-, and 4-parameter fits to static

dissolution test data at 40 °C and 90 °C for the 24 eLAW glasses; best fits to static dissolution test data at 40 °C and 90 °C for the 24 eLAW glasses and associated IGCM parameters are provided in the Supporting Information document.

REFERENCES

Åagaard, P., Helgeson, H.C. (1982) Thermodynamic and kinetic constraints on reaction rates among minerals and aqueous solutions. I. Theoretical considerations. American Journal of Science, 282: 237-285.

Abraitis, P.K., McGrail, B.P., Trivedi, D.P., Livens, F.R., Vaughan, D.J. (2000a) Single-pass flow-through experiments on a simulated waste glass in alkaline media at 40ºC. I. Experiments conducted at variable flow rate to glass surface area ratio. Journal of Nuclear Materials, 280: 196-205.

Abraitis, P.K., McGrail, B.P., Trivedi, D.P., Livens, F.R., Vaughan, D.J. (2000b) Single-pass flow-through experiments on a simulated waste glass in alkaline media at 40ºC. II. Experiments conducted with buffer solutions containing controlled quantities of Si and Al Journal of Nuclear Materials, 280: 206-215.

ASTM C1926-23 (2023) Standard Test Method for Measurement of Glass Dissolution Rate Using Stirred Dilute Reactor Conditions on Monolithic Samples. ASTM International, West Conshohocken, PA,

Crum, J.V., Reiser, J.T., Parruzot, B.P., Neeway, J.J., Bonnett, J.F., Kerisit, S.N., Cooley, S.K., Ryan, J.V., Smith, G.L., Asmussen, R.M. (2021) Seeded Stage III glass dissolution behavior of a statistically designed glass matrix. Journal of the American Ceramic Society, 104: 4145-4162.

Crum, J.V., Parruzot, B.P., Kerisit, S.N., Cooley, S.K., Song, X., Fang, Y., Ryan, J.V., Neeway, J.J., Bonnett, J.F., Daniel, R.C., Seymour, L.M., Reiser, J.T., Reyes, R.A., Burns, C.A., Smith, G.L., Asmussen, R.M. (2022) FY2022 Report: ILAW Glass Stage II and III Static Dissolution Testing and Modeling. RPT-IGTP-025 Rev. 1. PNNL-31758 Rev. 1. Pacific Northwest National Laboratory.

Doremus, R.H. (1964) Exchange and diffusion of ions in glass. Journal of Physical Chemistry, 68: 2212-2218.

Doremus, R.H. (1975) Interdiffusion of hydrogen and alkali ions in a glass surface. Journal of Non-Crystalline Solids, 19: 137-144.

Ebert, W.L., Bates, J.K., Buck, E.C., Bradley, C.R. (1992) Accelerated glass reaction under PCT conditions. MRS Online Proceedings Library, 294: 569-576.

Feng, X., Pegg, I.L., Guo, Y., Barkatt, A.A., Macedo, P.B. (1990) Effects of surface area-to-solution volume ratio on chemical durability of nuclear waste glasses. Materials Research Society Symposium Proceedings, 176: 383-392.

Frankel, G.S., Vienna, J.D., Lian, J., Guo, X., Gin, S., Kim, S.H., Du, J., Ryan, J.V., Wang, J., Windl, W., Taylor, C.D., Scully, J.R. (2021) Recent advances in corrosion science applicable to disposal of high-level nuclear waste. Chemical Reviews, 121: 12327-12383.

Frugier, P., Gin, S., Minet, Y., Chave, T., Bonin, B., Godon, N., Lartigue, J.-E., Jollivet, P., Ayral, A., De Windt, L., Santarini, G. (2008) SON68 nuclear glass dissolution kinetics: Current state of knowledge and basis of the new GRAAL model. Journal of Nuclear Materials, 380: 8-21.

Frugier, P., Chave, T., Gin, S., Lartigue, J.-E. (2009) Application of the GRAAL model to leaching experiments with SON68 nuclear glass in initially pure water. Journal of Nuclear Materials, 392: 552-567.

Frugier, P., Minet, Y., Rajmohan, N., Godon, N., Gin, S. (2018) Modeling glass corrosion with GRAAL. npj Materials Degradation, 2: 35.

Gin, S., Abdelouas, A., Criscenti, L.J., Ebert, W.L., Ferrand, K., Geisler, T., Harrison, M.T., Inagaki, Y., Mitsui, S., Mueller, K.T., Marra, J.C., Pantano, C.G., Pierce, E.M., Ryan, J.V., Schofield, J.M., Steefel, C.I., Vienna, J.D. (2013) An international initative on long-term behavior of high-level nuclear waste glass. Materials Today, 16: 243-248.

Grambow, B. (1985) A general rate equation for nuclear waste glass corrosion. Materials Research Society Symposium Proceedings, 44: 15-27.

Grambow, B. (1987) Nuclear Waste Glass Dissolution: Mechanism, Model and Application. JSS-TR-87-02. Hahn-Meitner Institut Berlin GmbH.

Grambow, B., Müller, R. (2001) First-order dissolution rate law and the role of surface layers in glass performance assessment. Journal of Nuclear Materials, 298: 112-124.

Johnson, J., Anderson, F., Parkhurst, D.L. (2000) Database thermo.com.V8.R6.230, rev. 1.11. In: Laboratory, L.L.N. (Editor), Livermore, CA.

Kerisit, S.N., Bonnett, J.F., Cordova, E.A., Song, X., Fang, Y., Cooley, S.K., Neeway, J.J. (2021a) Alternative Approaches to Determining Kg and Modeling its Influence on ILAW Glass Corrosion. PNNL-28999 Rev. 1. RPT-IGTP-020 Rev. 1. Pacific Northwest National Laboratory.

Kerisit, S.N., Lonergan, C.E., Cooley, S.K., Song, X., Fang, Y., Asmussen, R.M., Smith, G.L. (2021b) Ion-Exchange Immobilized Low-Activity Waste Glass Rate Model Term. RPT-IGTP-022. PNNL-31746. Pacific Northwest National Laboratory.

Kerisit, S.N., Cooley, S.K., Crum, J.V., Lonergan, C.E., Neeway, J.J., Parruzot, B.P., Ryan, J.V., Asmussen, R.M., Smith, G.L., Brown, E.E., Mabrouki, R., Skeen, R.S., Swanberg, D.J. (2022) Correlating immobilized low-activity waste glass corrosion model parameters to glass composition. 22406. Waste Management Symposium Proceedings.

Lasaga, A.C. (1995) Fundamental Approaches in Describing Mineral Dissolution and Precipitation Rates. In: White, A.F., Brantley, S.L. (Eds.), Chemical Weathering Rates of Silicate Minerals. Mineralogical Society of America, Washington, D.C., pp. 23-86.

McGrail, B.P., Ebert, W.L., Bakel, A.J., Peeler, D.K. (1997) Measurement of kinetic rate law parameters on a Na-Ca-Al borosilicate glass for low activity waste. Journal of Nuclear Materials, 249: 175-189.

McGrail, B.P., Bacon, D.H., Icenhower, J.P., Mann, F.M., Puigh, R.J., Schaef, H.T., Mattigod, S.V. (2001) Near-field performance assessment for a low-activity waste glass disposal system: Laboratory testing to modeling results. Journal of Nuclear Materials, 298: 95-111.

Neeway, J.J., Kerisit, S., Gin, S., Wang, Z., Zhu, Z., Ryan, J.V. (2014) Low-temperature lithium diffusion in simulated high-level boroaluminosilicate nuclear waste glasses. Journal of Non-Crystalline Solids, 405: 83-90.

Neeway, J.J., Kerisit, S.N., Liu, J., Zhang, J., Zhu, Z., Riley, B.J., Ryan, J.V. (2016) Ion-exchange interdiffusion model with potential application to long-term nuclear waste glass performance. Journal of Physical Chemistry C, 120: 9374-9384.

Neeway, J.J., Asmussen, R.M., Parruzot, B.P., Cordova, E.A., Williams, B.D., Leavy, I.I., Stephenson, J.R., McElroy, E.M. (2017) FY2016 ILAW Glass Corrosion Testing with the Single-Pass Flow-Through Method. RPT-IGTP-013. PNNL-26169. Pacific Northwest National Laboratory, Richland, WA.

Neeway, J.J., Asmussen, R.M., Cordova, E.A., Lonergan, C.E., Williams, B.D., Leavy, I.I., McElroy, E.M. (2018a) FY2017 ILAW Glass Corrosion Testing with the Single-Pass Flow-Through Method. RPT-IGTP-015. PNNL-27098. Pacific Northwest National Laboratory, Richland, WA.

Neeway, J.J., Rieke, P.C., Parruzot, B.P., Ryan, J.V., Asmussen, R.M. (2018b) The dissolution behavior of borosilicate glasses in far-from equilibrium conditions. Geochimica et Cosmochimica Acta, 226: 132-148.

Neeway, J.J., Parruzot, B.P., Bonnett, J.F., Reiser, J.T., Kerisit, S.N., Ryan, J.V., Crum, J.V. (2020) Acceleration of glass alteration rates induced by zeolite seeds at controlled pH. Applied Geochemistry, 113: 104515.

Neeway, J.J., Kerisit, S.N., Leavy, I.I., Cordova, E.A., Escobedo, N.M., Parruzot, B.P., Crum, J.V., Asmussen, R.M., Smith, G.L. (2023a) Immobilized Low-Activity Waste Glass Corrosion Model: Establishing the Incongruent Dissolution Representation for Enhanced Waste Glass. RPT-IGTP-031. PNNL-34390. Pacific Northwest National Laboratory.

Neeway, J.J., Reiser, J.T., Kerisit, S.N., Reyes, R.A., Daniel, R.C., Smith, G.L., Asmussen, R.M., Parruzot, B.P., Crum, J.V. (2023b) Effect of composition on the corrosion behavior of 24 statistically-designed alkali-borosilicate waste glasses. Journal of Nuclear Materials, 586: 154674.

Ojovan, M.I., Pankov, A., Lee, W.E. (2006) The ion exchange phase in corrosion of nuclear waste glasses. Journal of Nuclear Materials, 358: 57-68.

Papathanassiu, A.E., Viragh, C., Muller, I.S., Pegg, I.L. (2017) FY2016 ILAW Glass SPFT Testing for Disposal at IDF. VSL-17R3860-1. Vitreous State Laboratory at the Catholic University of America, Washington, DC.

Parkhurst, D.L., Appelo, C.A.J. (2013) Description of input and examples for PHREEQC Version 3 - A computer program for speciation, batch-reaction, one-dimensional transport, and inverse geochemical calculations, U.S. Geological Survey Techniques and Methods.

Parruzot, B.P., Crum, J.V., Reiser, J.T., Neeway, J.J., Kerisit, S.N., Daniel, R.C., Bonnett, J.F., Reyes, R.A., Seymour, L.M., Burns, C.A., Ryan, J.V., Smith, G.L., Asmussen, R.M. (2022) Effect of zeolite type, temperature, and pH on Stage III glass alteration behavior for two nuclear waste glasses. Journal of Nuclear Materials, 567: 153717.

Patyn, J., Van Iseghem, P., Timmermans, W. (1990) The long-term corrosion and modelling of two simulated Belgian reference high-level waste glasses - Part II. MRS Online Proceedings Library, 176: 299-307.

Pierce, E.M., McGrail, B.P., Rodriguez, E.A., Schaef, H.T., Saripalli, K.P., Serne, R.J., Krupk, K.M., Martin, P.F., Baum, S.R., Geiszler, K.N., Reed, L.R., Shaw, W.J. (2004) Waste Form Release Data Package for the 2005 Integrated Disposal Facility Performance. PNNL-14805. Pacific Northwest National Laboratory, Richland, WA.

Pierce, E.M., McGrail, B.P., Valenta, M.M., Strachan, D.M. (2006) The accelerated weathering of a radioactive low-activity waste glass under hydraulically unsaturated conditions:

Experimental results from a pressurized unsaturated flow test. Nuclear Technology, 155: 149-165.

Ribet, S., Gin, S. (2004) Role of neoformed phases on the mechanisms controlling the resumption of SON68 glass alteration in alkaline media. Journal of Nuclear Materials, 324: 152-164.

Rieke, P.C., Kerisit, S., Ryan, J.V., Neeway, J.J. (2018) Adaptation of the GRAAL model of glass reactivity to accommodate non-linear diffusivity. Journal of Nuclear Materials, 512: 73-93.

Ryan, J.V., Kerisit, S.N., Parruzot, B.P., Reiser, J.T., Lumetta, N.A., Cooley, S.K., Schonewill, P.P., Bonnett, J.F., Cordova, E.A., Seymour, L.M., Asmussen, R.M., Smith, G.L. (2021) Stirred-reactor coupon analysis: Determination of glass composition effects on forward-rate model parameters. RPT-IGTP-024. PNNL-31072. Pacific Northwest National Laboratory, Richland, WA.

Techer, I., Advocat, T., Lancelot, J., Liotard, J.-M. (2000) Basaltic glass: Alteration mechanisms and analogy with nuclear waste glasses. Journal of Nuclear Materials, 282: 40-46.

Thorpe, C.L., Neeway, J.J., Pearce, C.I., Hand, R.J., Fisher, A.J., Walling, S.A., Hyatt, N.C., Kruger, A.A., Schweiger, M., Kosson, D.S., Arendt, C.L., Marcial, J., Corkhill, C.L. (2021) Forty years of durability assessment of nuclear waste glass by standard methods. npj Materials Degradation, 5: 61.

Van Iseghem, P., Grambow, B. (1987) The long-term corrosion and modelling of two simulated Belgian reference high-level waste glasses. MRS Online Proceedings Library, 112: 631.

Vienna, J.D., Ryan, J.V., Gin, S., Inagaki, Y. (2013) Current understanding and remaining challenges in modeling long-term degradation of borosilicate nuclear waster glasses. International Journal of Applied Glass Science, 4: 283-294.

Vienna, J.D., Neeway, J.J., Ryan, J.V., Kerisit, S.N. (2018) Impacts of glass composition, pH, and temperature on glass forward dissolution rate. npj Materials Degradation, 2: 22.

Viragh, C., Abramowitz, H., Muller, I.S., Papathanassiu, A.E., Pegg, I.L. (2017) FY2017 ILAW Glass SPFT Testing for Disposal at IDF: Glass IDF21-EC14. VSL-17R4320-1. Vitreous State Laboratory at the Catholic University of America, Washington, DC.

Viragh, C., Abramowitz, H., Muller, I.S., Papathanassiu, A., Pegg, I.L. (2018) FY2018 ILAW Glass SPFT Testing for Disposal at IDF: Glasses ORLEC46 and ORLEC52. VSL-18R4510-2. Vitreous State Laboratory at the Catholic University of America, Washington, DC.

Declarations of interest: none.